Atomic layer deposition of ZnO gas diffusion electrodes for tunable CO2 electroreduction in membrane electrode assemblies

Applied Catalysis B: Environment and Energy 401 (2027) 127355

Contents lists available at ScienceDirect

Applied Catalysis B: Environment and Energy

journal homepage: www.elsevier.com/locate/apcatb

Atomic layer deposition of ZnO gas diffusion electrodes for tunable CO_2 electroreduction in membrane electrode assemblies

Lovelle Rhoy Manpatilan [a,b,*], Samuele Porro [a], Micaela Castellino [a,b], Marco Allione [a], Alessia Fortunati [b], Alessia Bardazzi [c], Pieter Glatzel [c], Juqin Zeng [a,b], Stefano Bianco [a,**]

[a] Department of Applied Science and Technology, Politecnico di Torino, C.so Duca degli Abruzzi 24, Turin 10129, Italy
[b] Center for Sustainable Future Technologies, Istituto Italiano di Tecnologia, Via Livorno 60, Turin 10144, Italy
[c] European Synchrotron Radiation Facility, 71 avenue des Martyrs, Grenoble 38000, France

ARTICLE INFO

Keywords:
Zinc oxide
Atomic layer deposition
CO_2 reduction
Electrocatalysis
Gas diffusion electrode
Membrane electrode assembly

ABSTRACT

The electrochemical conversion of CO_2 to CO in membrane electrode assembly (MEA) electrolyzers using gas diffusion electrodes (GDEs) offers a sustainable and scalable pathway for carbon utilization. Here, we present a one-step atomic layer deposition (ALD) approach to prepare ZnO-based GDEs with tunable loadings and high selectivity toward CO. Increasing the number of ALD cycles raises the ZnO loading but progressively reduces the pore accessibility within the GDE. An optimal balance is achieved at 200 ALD cycles, delivering a peak CO faradaic efficiency (FE_{CO}) of 88% and a full-cell energy efficiency of 38% at −100 mA cm^{-2}. Crucially, the scalability of ALD is demonstrated through stable long-term testing, achieving 85% FE_{CO} in a 5 cm^2 MEA after 30 h, and 80% FE_{CO} in a 100 cm^2 MEA after 24 h. These results establish ALD as an effective and versatile strategy for fabricating high-performance ZnO electrodes for CO_2 electrolysis.

1. Introduction

As global efforts to reduce greenhouse gas emissions intensify, carbon dioxide (CO_2) remains a major contributor to climate change, particularly from industrial and transport sectors. Achieving the net-zero goals outlined in the Paris Agreement requires the rapid development of scalable technologies to lower atmospheric CO_2 levels [1,2]. Electrochemical CO_2 reduction (CO_2RR) offers a promising approach to convert CO_2 into value-added products, contributing to both carbon mitigation and industrial sustainability [3].

Among these valuable products is carbon monoxide (CO), which serves as a key intermediate in the production of synthetic fuels, chemicals, and other industrial products. The conversion of CO_2 into CO provides a path towards a circular carbon economy, where CO_2 emissions can be recycled and reused. Furthermore, this process can be integrated with renewable energy sources, promoting environmental sustainability, and reducing reliance on fossil fuels [4].

Metallic electrocatalysts such as gold and silver have been widely studied for the efficient electrochemical conversion of CO_2 to CO. However, the high cost, scarcity, and environmental impact of these precious metals raise the need for cheaper alternatives [5]. Zinc stands out as an electrocatalyst for CO production due to its abundance, low-cost, non-toxic nature, and high catalytic activity [6]. A variety of synthesis methods, such as sputtering [7], electrodeposition [8,9], precipitation [10–12], and hydro/solvothermal techniques [13,14], have been explored to produce Zn-based electrocatalysts with diverse morphologies and properties. Notably, atomic layer deposition (ALD) offers distinct advantages for scalable electrode design. ALD allows the facile deposition of conformal, ultrathin films with atomic-scale precision, crucial for optimizing catalyst properties [15]. This precision is particularly valuable for the coating of complex substrates like gas diffusion electrodes (GDEs) and carbon nanotubes [16,17].

ALD has been widely adopted to tailor diverse electrocatalysts including Cu for CO_2RR [16,18], Ir and MoS_2 for hydrogen evolution reaction [19,20], MnO_x and Co_9S_8 for oxygen evolution reaction and oxygen reduction reaction [21,22], and Pt for methanol and formic acid electrooxidation [23]. Given these advances, zinc oxide (ZnO) emerges as a promising material for ALD-based catalyst design. While ALD-ZnO has been widely explored in applications such as thin film transistors [24], solar cells [25], gas sensors [26], light-emitting diodes [27],

* Corresponding author at: Department of Applied Science and Technology, Politecnico di Torino, C.so Duca degli Abruzzi 24, Turin 10129, Italy.
** Corresponding author.
E-mail addresses: lovelle.manpatilan@polito.it (L.R. Manpatilan), stefano.bianco@polito.it (S. Bianco).

https://doi.org/10.1016/j.apcatb.2026.127355
Received 11 May 2026; Received in revised form 21 July 2026; Accepted 13 August 2026
Available online 13 August 2026

photocatalysis [28], and antibacterial coatings [29], its application in CO_2RR remains comparatively limited. Recent studies have primarily employed ALD-ZnO to modify Cu-based electrodes, rather than being systematically studied as a primary active catalyst [18,30].

In this work, we investigate ZnO-based GDEs fabricated by ALD with precise control over electrode properties. The materials are subjected to comprehensive physicochemical characterization, combined with detailed electrochemical testing and operando studies, to elucidate the relationship between structural properties and catalytic performance in CO_2-to-CO conversion. These insights provide a foundation for the rational optimization of ZnO GDEs and extend to the design of other ALD-fabricated GDE systems.

2. Experimental

2.1. Fabrication and growth of ZnO electrodes

To prepare ZnO electrodes, ALD (Beneq TFS 200) of ZnO was performed onto commercial gas diffusion layers (GDL). The carbon-based GDL substrate (Sigracet 28 BC, Ion power GmbH) is composed of a hydrophobic microporous layer treated to 5% poly(tetrafluoroethylene) (PTFE) and a macroporous carbon fiber backing paper. Si(100) wafers (Si-Mat) were used as planar reference substrates to evaluate ZnO growth and saturation behavior by spectroscopic ellipsometry (Alpha-SE J.A. Woollam).

Diethyl zinc (DEZ, ≥99%) and deionized water (H_2O) were used as metal and oxygen precursors, respectively, while N_2 served as the purge gas. All depositions were carried out at a substrate temperature of 160 °C, reactor pressure of 1 mbar, and with precursors maintained at room temperature. Saturation behavior was assessed by varying one precursor pulse or purge step at a time while keeping all other process parameters (pulse/purge times, temperature, pressure, and number of cycles) constant. The corresponding ZnO film thicknesses on Si were calculated using a Cauchy model through the CompleteEASE software.

The optimized ALD sequence comprises of 0.2 s DEZ pulse – 2 N_2 purge – 0.5 s H_2O pulse – 2 s N_2 purge. Film thickness was monitored over 25–1000 cycles using this optimized sequence applied for GDL deposition. Samples are labeled ZnO-X, where X represents the cycle numbers of 50, 100, 200, 500, and 1000. The catalyst mass loading on the GDL was calculated from the mass difference before and after deposition.

2.2. Physicochemical characterization

X-ray diffraction (XRD) was performed using a PANalytical Empyrean X-ray diffractometer equipped with a PixCel3D Medipix detector and a Cu Kα radiation source (Ni-filtered, λ = 1.54178 Å), operated at 40 kV and 40 mA. Data were collected over a 2θ range of 20–70° with a step size of 0.026° in Bragg–Brentano geometry. Water contact angle measurements were carried out on Biolin Scientific Attension Theta Flex Tensiometer. Raman spectroscopy was implemented using a Renishaw inVia Reflex micro-Raman spectrophotometer with a cooled charge-coupled camera and a 514.5 nm solid-state laser excitation source.

Electrode morphology was examined using a field emission scanning electron microscope (FESEM, Supra 40, Zeiss), with an energy-dispersive X-ray spectroscopy (EDX) system (Oxford, liquid N_2-cooled Si-Li detector) for qualitative chemical composition analysis. Cross-sections were examined using a dual beam focused-ion beam-scanning electron microscope (FIB-SEM, TESCAN Solaris X) equipped with EDX (Oxford). A protective Pt layer was deposited on the surface of the ZnO layer, followed by Xe plasma FIB milling with stepwise reduction of the ion current from 5 nA to 250 pA to obtain the cross-sections. A thin portion of the sample deposited on Si was extracted using FIB-SEM. The portion, once attached to a standard copper lift-out grid (Omniprobe), was further thinned down to electron transparency to a final thickness around or slightly below 50 nm, using an ion beam with progressively reduced currents down to a final value of 20 pA. Finally, a gentle polishing step using low energy ions was applied to both sides of the obtained lamella (3 kV, 100 pA) to remove any residual damaged layer caused by the impact of high energy ions. The final lamella was then transferred into a transmission electron microscope (TEM, TALOS F200X from Thermo Fisher Scientific). High angle annular dark field (HAADF) scanning TEM (STEM) images and EDX mapping of the sample cross section along with high-resolution TEM (HRTEM) images were acquired with this machine using 200 kV of electron accelerating voltage.

X-ray photoelectron spectroscopy (XPS) analyses were carried out using a PHI 5000 VersaProbe II instrument equipped with a monochromatic Al Kα radiation source. Surface charge neutralization was obtained through a dual compensation system employing low-energy electrons together with Ar^+ ions. Survey spectra were collected over the 1200–0 eV binding energy range using a pass energy of 187.85 eV, a step size of 0.8 eV, a dwell time of 20 ms, and an X-ray beam diameter of 100 μm. High-resolution spectra were acquired within the 50–20 eV range using a pass energy of 23.50 eV, a step increment of 0.1 eV, a dwell time of 50 ms, and the same 100 μm spot size. Binding energies were calibrated by setting the C–C component of the C 1s signal, associated with adventitious carbon contamination, to 284.8 eV. Spectral processing and fitting were performed with CasaXPS (version 2.3.27).

2.3. Electrochemical characterization

The CO_2RR performance was first evaluated in a commercial transparent three-compartment flow cell (ElectroCell A/S) which allows for the visualization of the gas side of the GDE. The fabricated ZnO GDEs (1 cm^2 geometric area) served as the working electrode, a Pt-coated Ti plate (ElectroCell A/S) as the counter electrode, and a mini-Ag/AgCl (3 M Cl^-, 1 mm, leak-free LF−1) as the reference electrode. A Sustainion ® X37 50 RT anion exchange membrane (AEM, Dioxide materials) separated the catholyte and anolyte compartments, while the GDE separated the catholyte and gas compartments. A 1 M potassium hydroxide (KOH) aqueous solution was used for the anolyte and catholyte, and CO_2 was used for the gas side. A schematic is shown in Figure S1, with additional details in the supporting information (SI).

The CO_2RR performance was further assessed in a commercial membrane electrode assembly cell (MEA, Fuel cell store) with a 5 cm^2 active area and gold-plated stainless-steel endplates. The anode consisted of an IrO_2-coated Ti mesh anode (Shouyiji), while the cathode comprised the ZnO GDEs with a 5 cm^2 active area. A Sustainion X37–50 ® AEM was used as the separator and a 0.01" PTFE gasket employed for sealing. A 0.1 M potassium bicarbonate ($KHCO_3$) aqueous solution was used as the anolyte, while CO_2 was continuously fed to the cathodic compartment. The electrochemical tests were run using a Biologic SP−300 potentiostat equipped with a 10 A booster. Chronopotentiometry was performed at current densities between 100–300 mA cm^{-2}. A schematic is shown in Figure S2, with additional details in the SI including the scale-up measurement using a 100 cm^2 MEA cell.

Gas-phase products were quantified online using a micro gas chromatograph (μGC, Fusion®, INFICON) equipped with two channels: a 10 m Rt-Molsieve 5 A and an 8 m Rt-Q-Bond column, each coupled to a micro thermal conductivity detector. For all measurements, the outlet gas flow values were used for computing the faradaic efficiency (FE). Liquid products were analyzed by high-performance liquid chromatography (HPLC, Shimadzu Prominence) using a ReproGel column and a UV-Vis detector. The detection wavelength was set to 208 nm, corresponding to the maximum absorption of formic acid/formate. As a mobile phase, a 5.0 mM H_2SO_4 aqueous solution was used at 1.0 mL min^{-1} and 60°C. The FE of each product was calculated from Eq. 1.

$$FE = \frac{n \times N \times F}{Q} \times 100\% \quad (1)$$

Where n is the number of electrons required to obtain one mole of the product (n =2 for CO, H_2, $HCOO^-$), N is the number of moles of the product, F is the Faraday constant at 96485 C mol^{-1}, and Q is the total charge consumed during the corresponding electrolysis period.

2.4. Operando characterization

Operando high-energy-resolution fluorescence-detected X-ray absorption near edge structure (HERFD-XANES) measurements at the Zn K-edge were performed at beamline ID26 of the European Synchrotron Radiation Facility (ESRF, Grenoble, France). The operando measurements were carried out using a custom-built MEA with an active electrode area of 5.3 cm^2. The cell is equipped with two Kapton-sealed X-ray access windows (7.7 mm × 1.3 mm slits) covering the CO_2 serpentine flow field in direct contact with the gas-facing side of the GDE. A detailed description of the cell design will be provided in a separate forthcoming publication.

Spectra were collected under different experimental conditions, including before reaction (ex-situ), at open-circuit voltage (OCV) before CO_2RR, under applied cathodic bias of −50 mA cm^{-2} and −100 mA cm^{-2}, and at OCV after CO_2RR. The recorded energy range was from 9650 to 9780 eV. All spectra were further normalized to the area as determined for the full energy range. The spectrum of the Zn foil reference was not corrected for over-absorption as the spectral distortions do not affect the conclusions drawn in this work. Additional details are described in the supporting information.

3. Results and discussion

3.1. ALD ZnO growth on Si(100) as a benchmark

Spectroscopic ellipsometry was first used to evaluate the ZnO ALD growth regime and saturation behavior on planar Si(100) substrates. By systematically varying precursor pulse and purge durations, self-limiting behavior was observed at 0.05–0.4 s DEZ pulse times (Fig. 1a), 0.1–0.5 s H_2O pulse times (Fig. 1b), and 0.5–2.0 s N_2 purge times (Fig. 1c), corresponding to a stable growth per cycle (GPC) of 1.6–1.7 Å per cycle. Using the optimized ALD sequence described in section 2.1, a clear linear relationship between ZnO film thickness and ALD cycle number was observed from 25 to 1000 cycles (Fig. 1d). The thickness scaled linearly from 2.4 to 175 nm, with a GPC of 1.72 Å per cycle, consistent with several reports [24,31]. To verify the film thickness, a cross-sectional lamella of the 200-cycle sample (ZnO−200) was analyzed using HAADF-STEM-EDX (Fig. 1e). The measured ZnO thickness at 34 nm ± 2 nm agreed closely with the ellipsometry value of 32 nm ± 1 nm, indicating uniform film formation across the probed region.

3.2. Growth and characterization of ALD ZnO on GDL

Having established well-controlled ALD growth on Si(100), the optimal ALD sequence was applied to porous carbon-based GDL substrates. As shown in Fig. 2a, the catalyst loading increases approximately linearly from 50 to 200 cycles (0.18 mg cm^{-2} to 1.06 mg cm^{-2}). Further increasing the number of cycles leads to a pronounced deviation from linear scaling, as the loading increases only to 2.04 mg cm^{-2} at 500 cycles and 2.36 mg cm^{-2} at 1000 cycles. This behavior suggests that the incremental mass deposited per cycle becomes progressively lower in the porous substrate beyond a certain number of cycles.

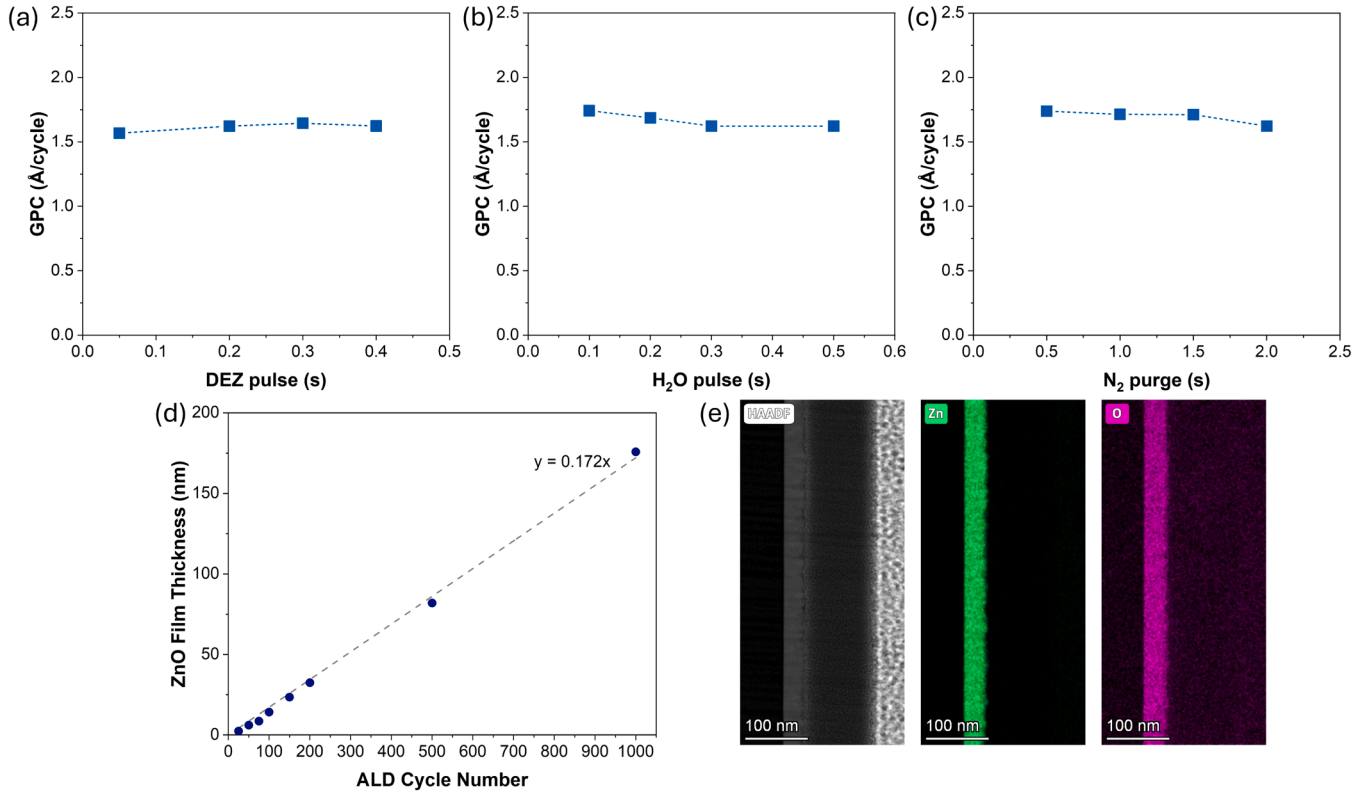

Fig. 1. Saturation curves for each ALD step of ZnO on Si(100) at 200 cycles: (a) DEZ pulse length at fixed 0.5 s H_2O pulse and 2 s N_2 purge, (b) H_2O pulse length at fixed 0.2 s DEZ pulse and 2 s N_2 purge, and (c) N_2 purge length at fixed 0.2 s DEZ pulse and 0.5 s H_2O pulse. (d) ZnO film thickness on Si(100) [y] as a function of ALD cycle number [x]. (e) HAADF-STEM-EDX of ZnO−200 in Si.

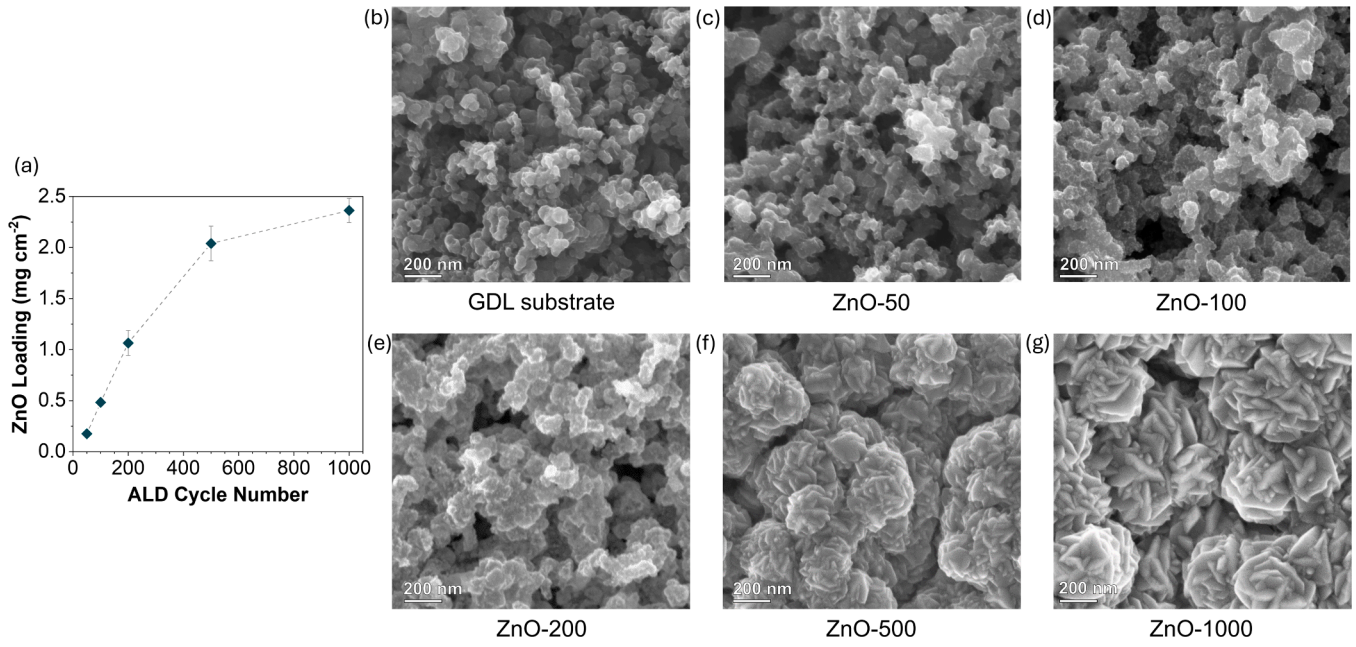

Fig. 2. (a) ZnO mass loading on GDL substrate vs. ALD cycle number (the error bars represent standard deviation among three samples). Surface FESEM images of (b) bare GDL substrate, (c) ZnO−50, (d) ZnO−100, (e) ZnO−200, (f) ZnO−500, and (g) ZnO−1000 GDEs.

To provide structural context for the observed growth behavior, the surfaces of the ZnO GDEs were examined using FESEM (Fig. 2b–g). The images reveal progressive growth of ZnO nanoparticles on the GDL with increasing cycle number. Minimal evidence of deposition is observed for ZnO−50 (Fig. 2c) compared to the bare GDL surface (Fig. 2b). However, EDX analysis confirms early-stage deposition; while the GDL exhibits only characteristic C and F peaks, distinct Zn signals appear in the EDX spectrum and elemental map of ZnO−50 (Figure S3). As the cycles progress to 100, a sparse distribution of ZnO nanoparticles around the carbon particles can be observed (Fig. 2d), which becomes more pronounced in ZnO−200 (Fig. 2e). At 500 cycles (Fig. 2f), the surface evolves into a rough, flower-like morphology, which grows larger in ZnO−1000 (Fig. 2g). With increasing cycles (500 and 1000), the underlying microporous network of the GDL is largely covered by the ZnO nanoparticles, whereas in the lower cycles, the pore structure remains clearly visible (50 and 100).

The morphological evolution aligns with the water contact angle results (Figure S4). The GDL substrate is inherently hydrophobic (> 150°) due to its PTFE content, which remains unchanged after ZnO−100 deposition, suggesting minimal surface coverage. With ZnO−200 and higher cycles, increasing coverage of intrinsically hydrophilic ZnO nanoparticles [32] significantly reduces the contact angle near 50°, reflecting a shift to hydrophilic surfaces.

Cross-sectional FIB-SEM analysis was performed on ZnO−100, ZnO−200, and ZnO−500 to assess the depth-dependent distribution of the catalysts within the GDL. Backscattered electron images (Fig. 3a, d, g) reveal the progressive evolution of ZnO deposition with increasing cycle number, while the corresponding EDX maps (Fig. 3b, e, h) show the extent of Zn penetration within the porous substrate. Importantly, these results demonstrate that ALD enables non-line-of-sight precursor infiltration rather than deposition confined to the external surface [16].

For ZnO−100, the morphology of the microporous layer is largely preserved (Fig. 3a). This is in agreement with the surface image (Fig. 2d), indicating minimal structural modification at low cycle numbers. Zn is detected beyond ~10 μm below the surface, with a higher apparent concentration within the top ~6 μm (Fig. 3b), suggesting effective precursor penetration on the carbon framework. For ZnO−200, deposition is detected within the top ~5 μm, with an evident concentration of coatings within the top ~3 μm (Fig. 3d–e). This trend is further observed for ZnO−500, where thicker coatings are predominantly localized within the top ~5 μm (Fig. 3g-h) indicating progressively restricted access to the deeper regions of the porous network.

Higher-magnification images present a clear evolution in coating development, with no discernible continuous layers for ZnO−100 (Fig. 3c), whereas conformal coatings of 26–40 nm and 80–95 nm are measured for ZnO−200 (Fig. 3f) and ZnO−500 (Fig. 3i), respectively. The variation in coating thickness for each electrode arises from the complex three-dimensional architecture of the substrate. Nonetheless, these values are in good agreement with ellipsometry-derived thicknesses of 32 and 82 nm, respectively (Fig. 1d). The ZnO surface morphology observed in Fig. 2 is also preserved in the cross-sectional view for ZnO−200 and ZnO−500, confirming that the nanoscale features extend throughout the ZnO layer. Collectively, this evolution from deep infiltration to near-surface accumulation reflects a transition toward diffusion-limited growth due to progressive pore narrowing and reduced accessibility [33,34], as evidenced by the deviation in ZnO loading from linear scaling at higher cycles (Fig. 2a).

The XRD patterns in Fig. 4a reveal the deposition of the hexagonal close-packed wurtzite ZnO (JCPDS 36–1451) across all electrodes. With increasing cycle number, the peaks gradually become more intense and sharper, indicating improved crystallinity and growth of larger ZnO domains with no preferential orientation. This evolution is consistent with FESEM imaging (Fig. 2c–g), which shows progressive nanoparticle coverage and morphological development on the GDL.

To provide direct atomic-scale validation of these findings, HR-TEM cross-sections were taken of the ZnO−200 Si sample (Figure S5). The images reveal a fully developed nanocrystalline morphology where distinct lattice fringes are clearly resolved throughout the film thickness. Specifically, the high-resolution view (Figure S5b–c) reveals a polycrystalline structure of randomly oriented nanodomains. The measured lattice spacings between 0.24 and 0.27 nm are consistent with the interplanar spacings of the (002), (101), and (100) planes of the wurtzite structure. The coexistence of these varying orientations validates the XRD observation of no preferential orientation. This structural assignment is further supported by Raman spectroscopy (Figure S6), where the characteristic E_2(high) peak [9] at 428–430 cm^{-1} confirms the wurtzite phase for ZnO−200, ZnO−500, and ZnO−1000 GDEs.

XPS was performed on ZnO−200 GDE (Fig. 4b–e) and ZnO−200 Si

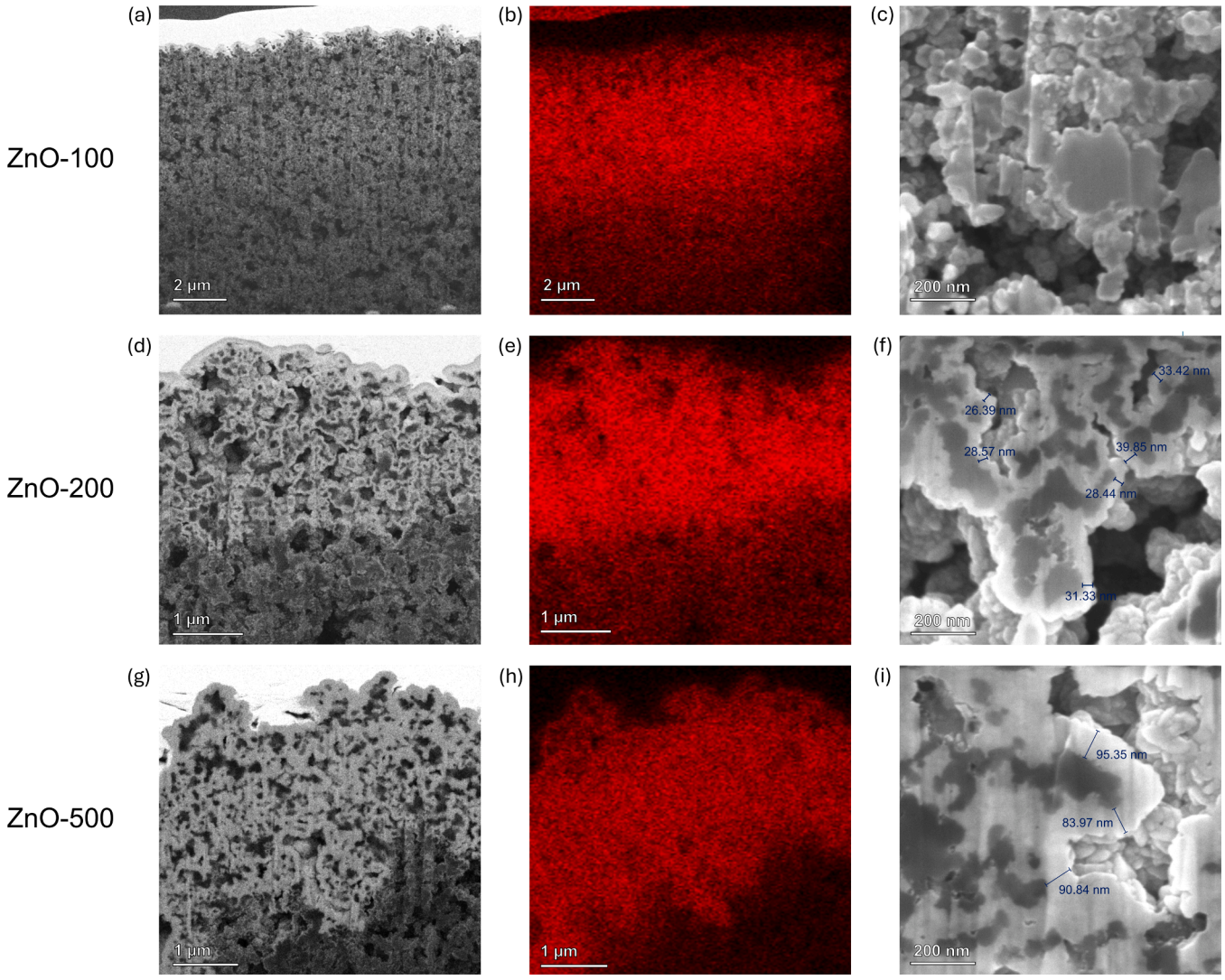

Fig. 3. Cross-section FIB-SEM images of ZnO−100 GDE with (a) backscattered electron setting and respective (b) Zn $L\alpha_{1,2}$ EDX map, and (c) higher-resolution secondary electron setting. Corresponding images are shown ZnO−200 GDE in (d), (e), (f) and ZnO−500 GDE in (g), (h), (i).

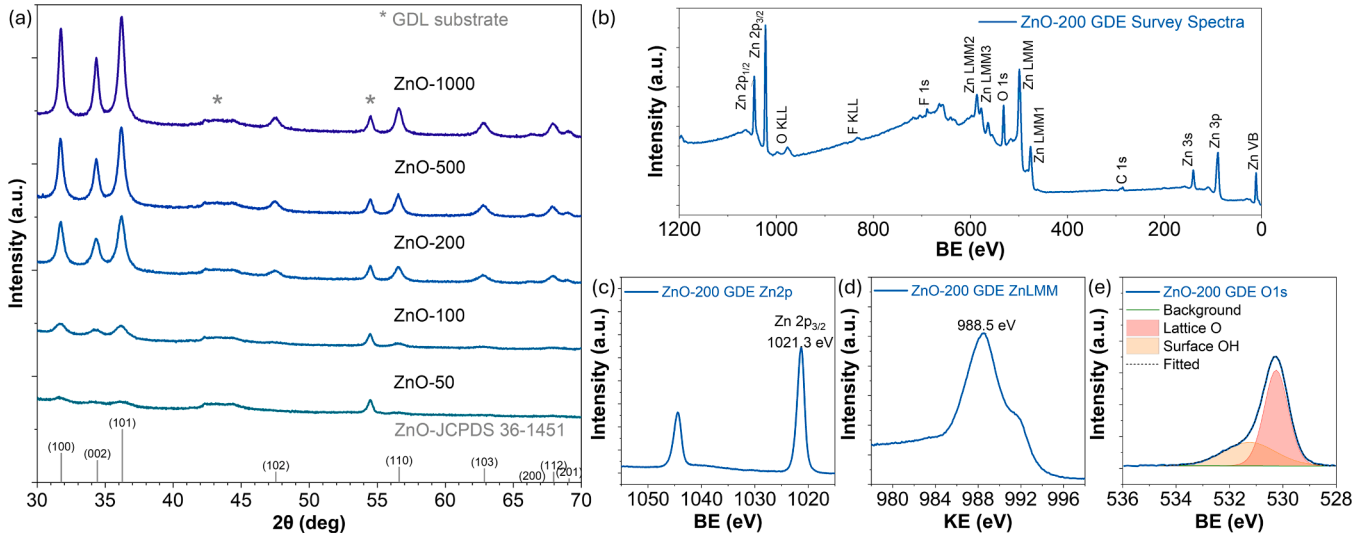

Fig. 4. (a) XRD spectra of ZnO GDEs. All XRD spectra were normalized with respect to the main substrate peak at 26° (not shown). XPS spectra of ZnO−200 GDE: (b) Survey, (c) Zn 2p, (d) Zn LMM, and (e) O 1s regions.

(Figure S7) to gain insights into the surface chemical composition. The survey spectrum shows Zn, O, C, and F peaks (Fig. 4b), contributed by the catalyst and GDL substrate. In the Zn 2p region (Fig. 4c), the Zn $2p_{3/2}$ peak is observed at 1021.3 eV; however, the exact chemical state is difficult to determine due to the similar binding energies of Zn species in this region. To resolve this, the Zn $L_3M_{4,5}M_{4,5}$ (LMM) Auger region was analyzed (Fig. 4d), revealing a main peak at 988.5 eV. The calculated modified Auger parameter (α') of this sample is 2009.8 eV, which corresponds to ZnO as shown on the Wagner plot (Figure S8). This assignment is further supported by the O 1s peak at 530.3 eV, Fig. 4e) which is characteristic of lattice oxygen, confirming the formation of ZnO in the GDE [35]. Similar spectral features for ZnO−200 Si indicate comparable Zn chemical states and ZnO formation across substrates.

3.3. Evaluation of CO_2RR

To establish the baseline CO_2RR performance, ZnO−100, ZnO−200, and ZnO−500 GDEs were selected as representative samples for chronopotentiometry in a 1 cm^2 3-compartment flow cell (Fig. 5a). At a current density of −200 mA cm^{-2}, all catalysts exhibit similar selectivity for CO (87% FE_{CO}) with minimal hydrogen production (8–10% FE_{H2}). Notably, ZnO−100 operates at a less negative cathode potential (−0.94 V vs. RHE) than ZnO−200 (−1.06 V) and ZnO−500 (−1.05 V). This indicates that increasing the increasing the ALD cycles beyond 100 does not lower the operational potential, suggesting that the additional catalyst mass in ZnO−200 and ZnO−500 does not improve active site utilization under these flow cell conditions.

Given the comparable CO selectivity across the three catalyst loadings, ZnO−200 GDEs were evaluated at various current densities for 1 h (Fig. 5b). CO production is already observed at −10 mA cm^{-2} with 85% FE_{CO}, while the highest FE_{CO} values (87–89%) are obtained at −50 to −200 mA cm^{-2}. Increasing the current density further to −250 to −300 mA cm^{-2} slightly decrease the FE_{CO}. The cathode potential becomes progressively more negative with increasing current density, shifting from −0.41 V at −10 mA cm^{-2} to −1.28 V vs. RHE at −300 mA cm^{-2}. For all tests, liquid products are negligible, with formate accounting for around 1% FE for most samples.

Based on these preliminary results, the study was expanded to include the full range of ZnO GDEs at selected current densities in a 5 cm^2 MEA cell. This transition to the MEA configuration was chosen to evaluate CO_2RR performance under more industrially relevant conditions, particularly given the gaseous nature of the products [3]. Prior to CO_2RR, an in-situ prereduction step was performed at −50 mA cm^{-2} for 3 min to reduce ZnO to its catalytically active metallic Zn phase [14].

At −100 mA cm^{-2} (Fig. 6a), all GDEs exhibit a high and nearly identical FE_{CO} (84–88%) and low FE_{H2} (4–7%), indicating that selectivity is independent of loading at low current densities. Increasing to −200 mA cm^{-2} (Fig. 6b) leads to a slight decline of FE_{CO} to 77–85%. However, at −300 mA cm^{-2} (Fig. 6c), loading-dependent behavior becomes pronounced. Low-loading electrodes (ZnO−50 and ZnO−100) show significantly decreased FE_{CO} (55%) with substantial increase in FE_{H2} (~30%) and cell voltages, along with large error bars indicative of instability and electrode flooding. In contrast, the higher-loading electrodes maintain more stable CO selectivity, with ZnO−200 reaching the highest FE_{CO} of 74%.

It can be observed that increasing the applied current density at a fixed CO_2 inlet flow rate of 25 standard cubic centimeters per minute (sccm) decreases the total FE of the gaseous products. This may be attributed to the enhanced generation of OH^- at the cathode that promotes the chemical conversion of CO_2 into (bi)carbonate species rather than electroreduction to gaseous products. This shift in local equilibrium toward carbonate formation, driven by higher OH^- concentration, reduces the availability of CO_2 for gas-phase product formation. This interpretation is consistent with reported increases in CO_3^{2-} formation under elevated current densities [36,37]. Increasing the inlet CO_2 flow rate to 50 sccm at −300 mA cm^{-2} (Fig. 6d) significantly improves CO selectivity across all electrodes, restoring FE_{CO} to ~80%, while decreasing the average cell voltages. This improvement can be attributed to enhanced CO_2 mass transport to the cathode, which mitigates local CO_2 depletion and reduces CO_2 loss.

Among all GDEs, ZnO−200 consistently exhibited the highest FE_{CO} from −100 to −300 mA cm^{-2}. Replicate CO_2RR measurements of this GDE (Figure S9) show excellent agreement in both the FE and cell voltages under identical operating conditions. The high reproducibility is aligned with the conformal and uniform ZnO deposition expected of the ALD process. For all measurements, the FE values stabilized after approximately 20 min, indicating that steady-state operation was reached before the reported values were averaged as shown in Fig. 6.

To validate the advantages of the ALD approach, control electrodes were prepared by drop-casting commercial ZnO nanoparticles (ZnO-NP) with comparable mass loadings and tested under identical CO_2RR conditions (−200 mA cm^{-2}). When comparing the morphology at a loading of ~1.0 mg cm^{-2}, the ALD GDE (ZnO−200) yields a conformal ZnO coating directly on the carbon particles (Fig. 2e and Fig. 3d), whereas the drop-casted counterpart (ZnO-NP−1.0) clusters on the GDL surface (Figure S10a-b). At these similar loadings, ZnO−200 (Fig. 6b) outperforms ZnO-NP−1.0 (Figure S10c) with higher FE_{CO} (85% vs. 78%) and lower cell voltage (3.33 V vs. 3.51 V). While particle size differences in the commercial benchmark may contribute to this gap, the drop-casted GDEs require double the loading (2.0 mg cm^{-2}) to achieve 85% FE_{CO} yet still operate at a higher voltage (3.38 V). This demonstrates that the improved performance is largely driven by the structural and interfacial advantages of the conformal ALD methodology.

To estimate the relative electrochemically active surface area (ECSA)

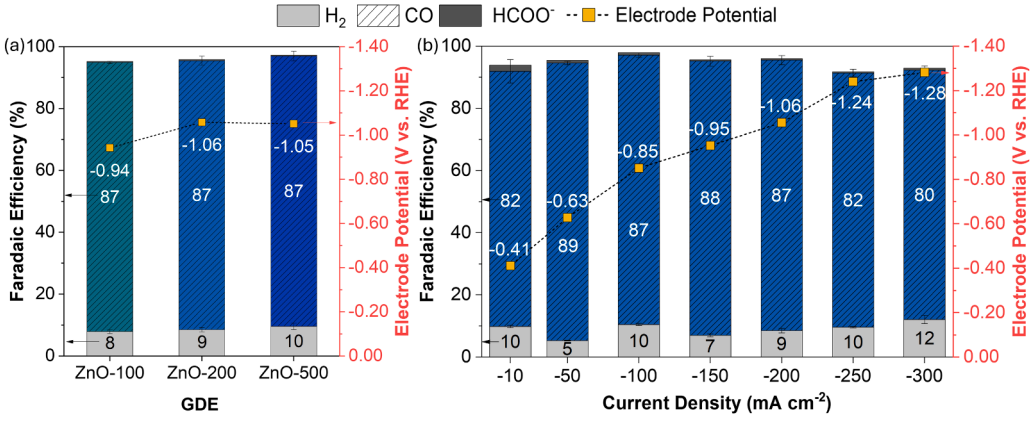

Fig. 5. Average FE and cathode potential (non-IR corrected) of (a) ZnO−100, ZnO−200, and ZnO−500 at −200 mA cm^{-2} and (b) ZnO−200 at various current densities in a 1 cm^2 flow cell at 1 M KOH. The error bars represent the standard deviation among consecutive GC measurements from 20 to 60 min testing window.

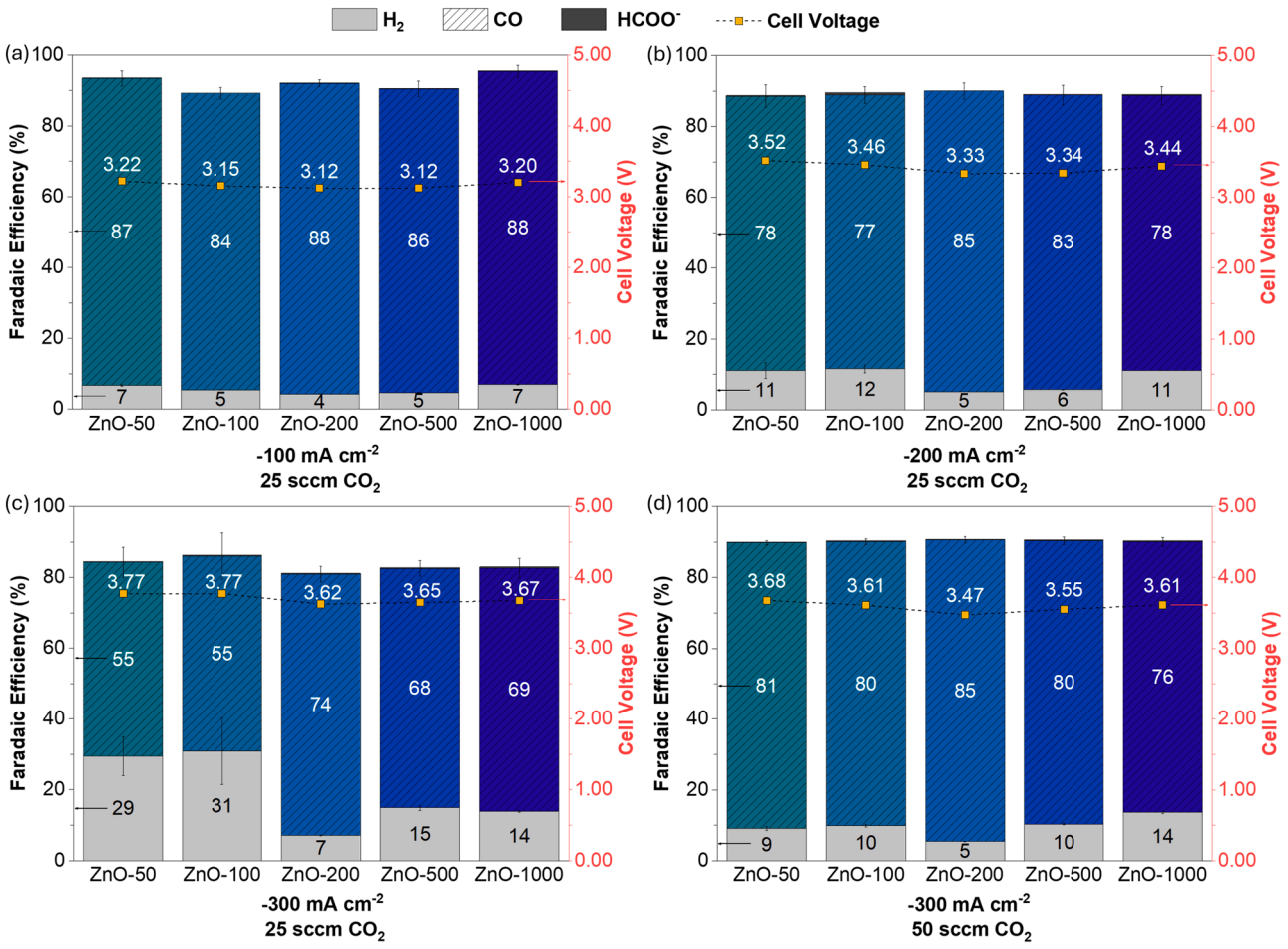

Fig. 6. Average FE distribution and cell voltages of ZnO GDEs at applied current densities of (a) −100, (b) −200 and (c) −300 mA cm^{-2} with a 25 sccm CO_2 inlet flow, and (d) −300 mA cm^{-2} at 50 sccm CO_2 in a 0.1 M $KHCO_3$, 5 cm^2 MEA cell. Error bars represent the standard deviation among consecutive GC measurements from 20 to 60 min testing window.

across the GDEs, the double layer capacitance (C_{dl}) was obtained from cyclic voltammetry (Figure S11). ZnO−50 exhibits the lowest C_{dl} of 47 μF cm^{-2}, followed by ZnO−100 with 165 μF cm^{-2}, while ZnO−200 and ZnO−500 show higher values of 463 and 478 μF cm^{-2}, respectively. However, a further increase to 1000 cycles reduced the C_{dl} to 276 μF cm^{-2} (Fig. 7a). These results correlate with the physical growth regimes observed in the ZnO loading, surface morphology (Fig. 2), and cross-sectional analyses (Fig. 3). The increase in ECSA in low-to-moderate cycles (up to 200) reflects the successful conformal infiltration of active material across the carbon framework while fully preserving its open pore structure. The plateau at 500 cycles and subsequent drop at 1000 cycles are practical results of shifting into a diffusion-limited growth regime. As observed in the cross-sections, the progressive thickening of the conformal layer at high cycle numbers narrows the local pore channels that restrict electrolyte and ion access to the deeper parts of the electrode. Thus, the C_{dl} trend reveals that an intermediate ALD cycle number provides the most favorable balance between maximizing active surface area coverage and keeping the pore structure open for transport.

The underlying kinetics were evaluated using potentiostatic electrochemical impedance spectroscopy (EIS) for ZnO−100, ZnO−200, and ZnO−500 at 2.8, 3.0, and 3.2 V (Fig. 7b). These potentials primarily represent low current densities (up to −100 mA cm^{-2}), allowing for characterization of the intrinsic kinetics before severe transport limitations occur. As summarized in Table S1, the fitted charge-transfer resistance (R_{ct}) values drop significantly for all samples as the voltage increases, demonstrating accelerated reaction kinetics at higher potentials. Across every voltage step, ZnO−200 exhibits the smallest semi-circle diameters, reaching its lowest R_{ct} of 0.42 Ω at 3.2 V. This confirms an optimal synergy between loading and site accessibility. Conversely, the higher resistance of ZnO−100 (0.67 Ω at 3.2 V) and ZnO−500 (0.49 Ω at 3.2 V) point to insufficient loading and film-induced transport barriers, respectively. Although ZnO−500 exhibits a slightly higher ECSA than ZnO−200 (Fig. 7a), its consistently higher R_{ct} values suggest that a portion of its surface area becomes less accessible under dynamic operating conditions. As the thicker ALD film narrows the internal pore channels, it can restrict the local transport for reactants and electrolyte ions within the GDE, thereby limiting catalyst layer utilization and inflating the apparent charge-transfer resistance.

The impact of these differences in ECSA and charge-transfer resistance becomes clear when analyzing the CO production rates (Fig. 7c) and CO_2 single-pass conversion (SPC) values (Fig. 7d). At −100 and −200 mA cm^{-2}, CO production and SPC scaled proportionally with current density, confirming that the CO_2 supply was sufficient to sustain the reaction. At −300 mA cm^{-2} and 25 sccm CO_2, both metrics diverge strongly with ZnO loading. Within these conditions, a clear maximum is observed at ZnO−200, with a CO production rate of 4.1 mmol h^{-1} cm^{-2} and SPC of 31%. Lower-loading electrodes (ZnO−50 and ZnO−100) show reduced CO production and SPC (~23%). In contrast, higher-loading electrodes (ZnO−500 and ZnO−1000) maintain relatively high CO production but do not further improve SPC (~28–29%). When CO_2 flow is increased to 50 sccm, CO production increases up to 4.7 mmol h^{-1} cm^{-2}, while SPC decreases to ~16–17% and becomes largely independent of loading. This suggests that increased CO_2

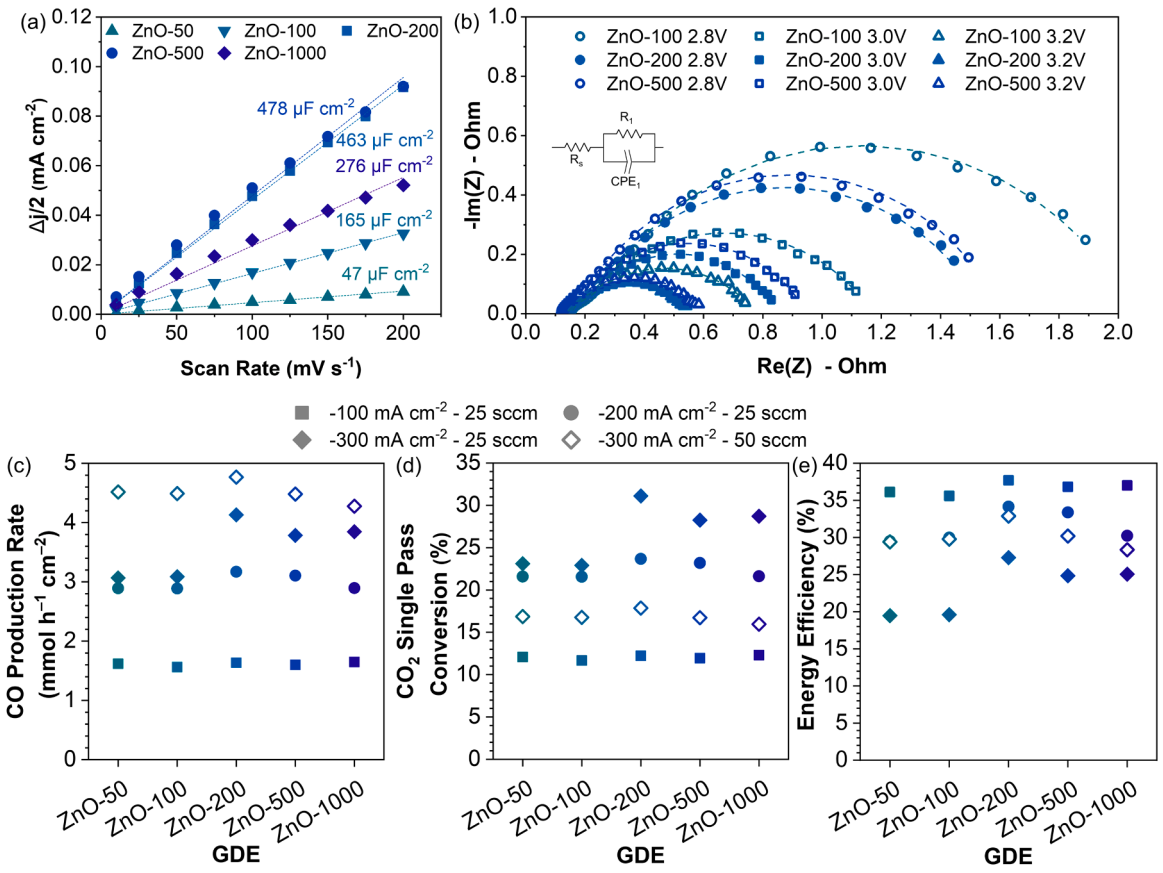

Fig. 7. (a) Double layer capacitance values from cyclic voltammetry of ZnO GDEs in N_2-saturated 0.1 M $KHCO_3$. (b) Potentiostatic electrochemical impendance spectra of ZnO−100, ZnO−200, and ZnO−500 GDEs at 2.8 V, 3.0 V, and 3.2 V using 5 cm^2 MEA (dashed lines are fitted spectra from the shown equivalent circuit). (c) CO production rates, (d) CO_2 single pass conversion, and (e) energy efficiency values from 5 cm^2 MEA measurements.

availability shifts the system toward higher throughput at the expense of per-pass utilization, while loading plays a reduced role in determining performance.

These cumulative advantages in kinetics and selectivity translate directly to the energy efficiency (EE) values (Fig. 7e), where ZnO−200 achieves the highest EE across the tested current densities. The efficiency peaks at 38% under low-to-moderate currents (−100 and −200 mA cm^{-2}). Even at the mass transport-limited regime of −300 mA cm^{-2} with 50 sccm CO_2, ZnO−200 maintains superior efficiency of 33% compared to under-loaded or over-coated variants. This confirms that balancing ECSA, charge transfer resistance, and reactant supply optimize cell-level energy conversion.

Collectively, these findings point to a clear trade-off in electrode design and CO_2 utilization. While low-loading GDEs are efficient at moderate current densities, higher throughput necessitates an optimal catalyst loading such as ZnO−200 to sustain high current density and CO selectivity. This reflects the precision of ALD in tuning the balance between active site density and CO_2 transport. Beyond this optimal point, thicker films offer diminishing gains due to increased kinetic resistance and reduced accessibility. Ultimately, ZnO−200 stands out as the best performing electrode, providing the most effective balance of kinetic activity and reactant delivery under high-flux conditions.

The ZnO−200 GDE was then evaluated for stability measurements at −100 mA cm^{-2} in both 5 cm^2 (Fig. 8a) and 100 cm^2 (Fig. 8b) MEA

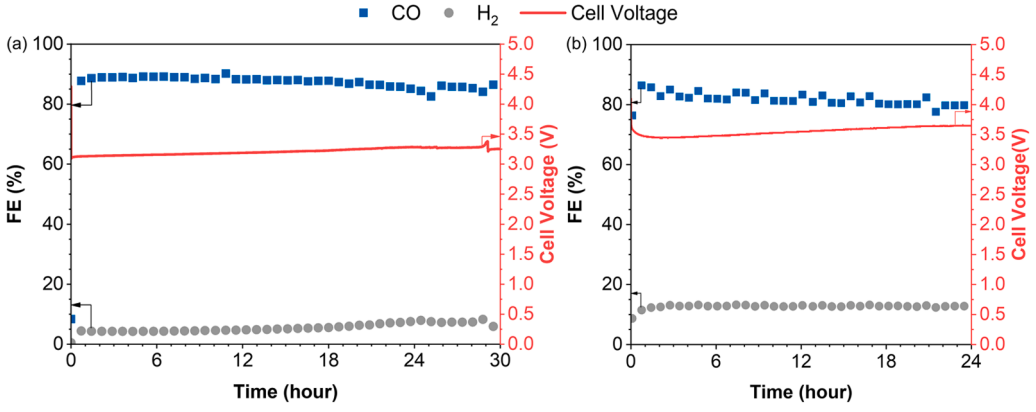

Fig. 8. Stability tests of ZnO−200 at −100 mA cm^{-2} using (a) 5 cm^2 and (b) 100 cm^2 MEA cells. FE_{HCOO^-} is less than 0.5% for both measurements.

configurations. In the 5 cm^2 cell, the electrode demonstrated excellent stability, maintaining over 85% FE_{CO} throughout 30 h of continuous operation. For reference, ZnO−100 also exhibited stable operation under the same conditions, maintaining ~80% FE_{CO} up to 30 h (Figure S12). Upon scaling up to the 100 cm^2 MEA, ZnO−200 delivered a maximum of ~87% FE_{CO} at the first hour and sustained ~80% FE_{CO} after 24 h of operation, confirming that the catalyst remains active and selective even upon a 20-fold scale up. These results demonstrate that the 5 cm^2 MEA serves as a useful benchmark for assessing catalyst stability, while the 100 cm^2 validates its potential for larger-scale operation.

In comparison with other Zn-based electrodes summarized in Table S2, the ALD ZnO GDEs show competitive performance, delivering a stable 85% FE_{CO} for 30 h at −100 mA cm^{-2}, with a cell voltage of 3.2 V, and a full-cell EE of 36%. This compares favorably to other Zn-based systems, which exhibit FE_{CO} between 70–94%, cell voltages between 2.7–3.5 V, EEs between 31–41%, and stabilities reaching up to 100 h [11]. Furthermore, this work stands out as one of the few studies to successfully evaluate Zn-based electrodes at a large-scale 100 cm^2 MEA configuration, demonstrating a significant step toward practical scalability.

Despite this progress, a considerable performance gap remains to state-of-the-art systems based on Ni single-atom catalysts, and Ag and Au-based electrodes. These materials achieve higher selectivity (>90% FE_{CO}) and EE (32–53%), lower cell voltages (down to 2.25 V), and in some cases, exceptional durability (e.g., up to 4500 h for Ag nanoparticles in a 100 cm^2 MEA at −100 mA cm^{-2}), though it is worth noting that reaching these superior values often requires specific set-up or process modifications (such as acid humidification of the CO_2 feed) [38]. Nevertheless, these systems currently represent the benchmark in the field.

3.4. Operando and postmortem characterization

In this work, operando HERFD-XANES was performed for ZnO−200 GDE in a customized MEA cell to track the real-time reduction process and identify the prevailing Zn oxidation states during CO_2RR. As shown in Fig. 9a, inserting the GDE into the cell introduces a pronounced change in spectral features even at OCV (denoted as OCV before CO_2RR). Specifically, a slight shift of the edge toward higher energies relative to the pristine GDE is observed. This modification suggests a change in the local electronic and coordination environment of Zn upon exposure to CO_2 and $KHCO_3$ electrolyte in the cell prior to electrochemical polarization. This shift may be associated with the formation of surface carbonate or hydroxycarbonate species, although the exact nature of the corresponding Zn species cannot be determined in the absence of suitable reference spectra.

When applying a current of −50 mA cm^{-2}, a shift of the absorption edge toward lower energies is observed, indicating the electrochemical reduction of the ZnO precursor. This metallic character is maintained even as the current density is increased to −100 mA cm^{-2}, with the edge positions closely matching the Zn foil reference. We note that the Zn foil reference spectrum was not corrected for over-absorption effects that reduce the amplitude of the white line. Upon returning to open circuit conditions after electrolysis (OCV after CO_2RR), the absorption edge remains closely aligned the metallic reference, with a subtle shift toward

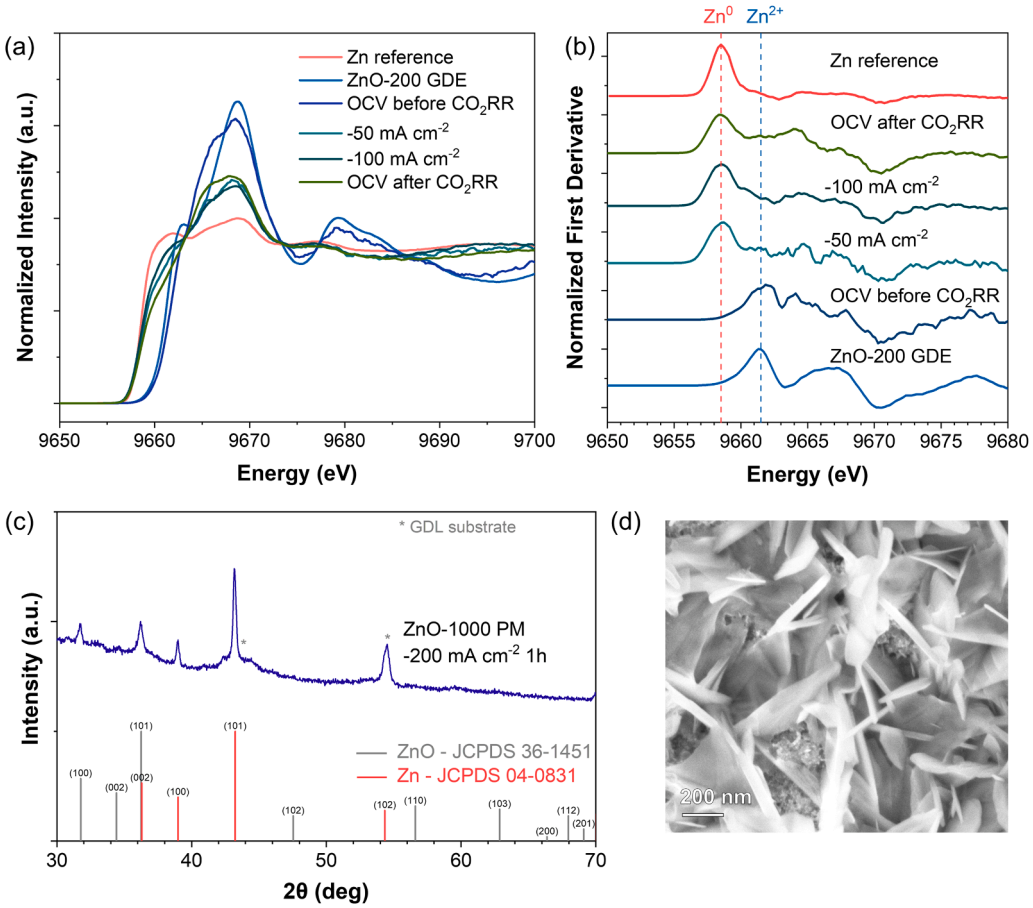

Fig. 9. (a) Operando HERFD-XANES spectra of ZnO−200 GDE at −50 mA cm^{-2} and −100 mA cm^{-2} set to normalized intensity, and (b) Corresponding first-order derivative of HERFD-XANES spectra. (c) XRD spectra of postmortem ZnO−1000 GDE after 1 h CO_2RR in 5 cm^2 MEA at −200 mA cm^2. (d) FESEM image of postmortem ZnO−1000 GDE.

higher energies.

This transition is further validated by the first derivative of the XANES spectra (Fig. 9b). A comparison of the derivative profiles reveals that the prominent derivative peak at ~9662 eV (corresponding to Zn^{2+} in the pristine and OCV before CO_2RR states) is entirely suppressed. In its place, a dominant peak emerges at ~9659 eV under cathodic bias, aligning precisely with the inflection point of the metallic foil. While the operando MEA environment introduces inherent signal fluctuations, the absence of any resolvable shoulders or residual features at the Zn^{2+} edge position suggests a near-complete electrochemical reduction of the ZnO−200 catalyst into a metallic Zn phase. At OCV after CO_2RR, while the primary derivative peak remains centered near the metallic Zn^0 reference, a noticeable broadening of the peak profile is observed between the 9660–9664 eV range compared to the previous biased state at -100 mA cm^{-2}. This suggests a minor re-oxidation of the Zn catalysts when returning to open circuit conditions, which may be attributed to the surrounding chemical environment within the MEA.

These findings indicate that the active phase under CO_2RR conditions is predominantly metallic Zn^0, which originates from the in-situ reduction of the ZnO precatalyst under cathodic polarization. Metallic Zn signatures are detected at the earliest available measurement (~8 min under -50 mA cm^{-2}), indicating that ZnO reduction has already occurred within the initial stages of CO_2RR operation. While the exact onset of this transformation cannot be resolved due to the limited time resolution of the early-stage operando measurements, these results confirm rapid structural evolution under reaction conditions. This aligns with reported phenomena in CO_2RR literature [9,12,14], where in-situ techniques such as Raman spectroscopy have frequently demonstrated the transformation of ZnO precursors into metallic active phases under reducing conditions. These dynamic structural transformations occur during the early stages of operation. Thereafter, the formation of stable metallic Zn sites underpins the sustained performance observed during long-term testing over tens of hours.

To further corroborate the operando findings, postmortem structural characterization was performed on ZnO−1000 after 1 h of CO_2RR at -200 mA cm^{-2}. The XRD pattern (Fig. 9c) confirmed the formation of metallic Zn with an hcp structure, indicating the reduction of ZnO under CO_2RR conditions. Weak reflections corresponding to ZnO were also detected, which may originate from partial surface re-oxidation during air exposure or incomplete reduction of ZnO to Zn [9]. Since ZnO−1000 possesses the highest catalyst loading among the investigated samples, the metallic Zn phase was more readily detectable by XRD compared to the lower-loading GDEs. In addition, partial catalyst delamination during membrane removal may have contributed to the relatively weak diffraction intensity observed. Postmortem FESEM imaging of ZnO−1000 (Fig. 9d) revealed dendritic structures formed after CO_2RR. Comparable Zn morphologies have been previously reported [9], that were attributed to a dissolution-redeposition process. These observations suggest that a comparable mechanism may contribute to the features observed in the ALD ZnO GDEs.

Postmortem evaluation was also performed on the stability-tested ZnO−200 GDEs from both the 5 cm^2 and 100 cm^2 MEAs (Figure S13). Surface FESEM imaging showed that the 5 cm^2 sample forms flake-like dendritic structures (Figure S13a), similar to ZnO−1000 (Fig. 9d). Conversely, the 100 cm^2 sample appears identical to the bare substrate (Figure S13e), suggesting severe catalyst delamination from membrane detachment. Despite this delamination, residual material was sufficient for XPS analysis, revealing a similar Zn^{2+} chemical state for both samples. The 5 cm^2 sample features a Zn $2p_{3/2}$ peak at 1022.5 eV (Figure S13b) and a Zn LMM peak at 986.8 eV (Figure S13c), yielding an α' of 2009.3 eV, which corresponds to varied species such as $Zn_5(OH)_6(CO_3)_2$, $Zn(OH)_2$, and $ZnCO_3$ (Figure S8). The O 1s spectrum confirms this carbonate-rich phase via a dominant CO_3^{2-} peak at 532.4 eV alongside a minor lattice oxygen peak (Figure S13d) [39]. The 100 cm^2 sample exhibited nearly identical zinc core levels (Zn $2p_{3/2}$ at 1022.4 eV, Zn LMM at 986.8 eV, α' = 2009.2 eV), though its O 1s spectrum (Figure S13h) shows a combination of CO_3^{2-} and surface hydroxyls. While operando characterization proves that metallic Zn is the active phase during operation, these postmortem results indicate that the spent catalyst materials quickly revert to Zn^{2+} species upon reacting with the aqueous electrolyte, CO_2, or ambient air during cell disassembly.

Overall, the postmortem characterization results are in agreement with the HERFD-XANES analysis, collectively demonstrating that ZnO undergoes reduction to metallic Zn during CO_2RR. These dynamic transformations likely influence both catalyst stability and CO_2RR performance, highlighting the evolving nature of the Zn-based catalyst under operating conditions. It is anticipated that the highly uniform distribution and nanoscale thickness of the initial ALD structure ensure that the precatalyst is distributed evenly across the 3D matrix without blocking pores. Upon bias, this initial configuration likely guides the subsequent structural evolution, where the morphological reconstruction into dendritic structures appears to establish a network of active sites capable of sustaining high current densities. The presence of the carbonate-rich Zn^{2+} phase post-reaction indicates that the electrochemically formed metallic Zn^0 is highly prone to oxidation once the protective cathodic polarization is removed. This explains the highly dynamic behavior of the ALD-derived catalyst under operating conditions, where the in-situ stabilized metallic network enables the competitive faradaic efficiency and robust operational stability observed over tens of hours.

4. Conclusions

This work demonstrates ALD as a facile strategy for fabricating ZnO-based GDEs with precisely tunable catalyst loading in a freestanding architecture. By depositing ZnO directly throughout the porous substrate, this technique effectively increases active site density within the electrode. However, higher catalyst loading inherently reduces GDE porosity, creating a clear trade-off between catalytic activity and mass transport at elevated current densities. Through systematic control, the optimized ALD-derived ZnO electrode delivers high CO selectivity, energy efficiency, and promising scalability at industrially relevant current densities. Postmortem and operando characterizations indicate that ZnO is reduced to metallic Zn under CO_2RR conditions, which subsequently serves as the stable and active sites for the reaction.

More broadly, this work highlights the generality of the ALD technique as a scalable, binder-free, and versatile approach to fabricate a wide spectrum of electrocatalysts, enabling precise control over mass loading, and active architectures for diverse MEA-based CO_2RR applications.

Declaration of Competing Interest

The authors declare that they have no known competing financial interests or personal relationships that could have appeared to influence the work reported in this paper.

Acknowledgments

The authors acknowledge funding from the European Union Horizon 2021 programme under the Marie Skłodowska-Curie Doctoral Networks (MSCA-DN) ECOMATES under grant agreement No. 101072830. The authors also acknowledge the European Synchrotron Radiation Facility (ESRF) for provision of synchrotron radiation facilities under proposal ID IH-MA−804 and IH-MA−716 at beamline ID−26. The authors thank G. Cicero and V. Cauda from PoliTo for their support and assistance. The authors further acknowledge the Piemonte Quantum Enabling Technology laboratory, and particularly to R. Rocci, E. Cara, and M. Malerba of the Istituto Nazionale di Ricerca Metrologica, for their support. The authors also acknowledge L. Huang, A. Cardone, S. Quesada, F. di Costola, M. Bagheri, and J. Dangbegnon from IIT-CSFT for their

assistance in various experiments. Finally, the authors gratefully acknowledge the students of the Nanomaterials Engineering master's degree course (academic year 2025/2026) for their valuable contributions to the research activities concerning the materials investigated in this study.

Appendix A. Supporting information

Supplementary data associated with this article can be found in the online version at doi:10.1016/j.apcatb.2026.127355.

Data availability

Data will be made available on request.

References

[1] M. Filonchyk, M.P. Peterson, L. Zhang, V. Hurynovich, Y. He, Greenhouse gases emissions and global climate change: examining the influence of CO2, CH4, and N2O, Sci. Total. Environ. 935 (2024) 173359, https://doi.org/10.1016/j.scitotenv.2024.173359.

[2] Y. Sun, Y. Jiang, H. Wei, Z. Zhang, S. Irshad, X. Liu, Y. Xie, Y. Rui, P. Zhang, Nano-enabled strategies for greenhouse gases emission mitigation: a comprehensive review, Nano Today 57 (2024) 102378, https://doi.org/10.1016/j.nantod.2024.102378.

[3] S. Varhade, A. Guruji, C. Singh, G. Cicero, M. García-Melchor, J. Helsen, D. Pant, Electrochemical CO_2 reduction: commercial innovations and prospects, ChemElectroChem 12 (2025) e202400512, https://doi.org/10.1002/celc.202400512.

[4] F.-Y. Gao, R.-C. Bao, M.-R. Gao, S.-H. Yu, Electrochemical CO_2 -to-CO conversion: electrocatalysts, electrolytes, and electrolyzers, J. Mater. Chem. A 8 (2020) 15458–15478, https://doi.org/10.1039/D0TA03525D.

[5] N.B.D. Monti, M. Fontana, A. Sacco, A. Chiodoni, A. Lamberti, C.F. Pirri, J. Zeng, Facile fabrication of Ag electrodes for CO_2 -to-CO conversion with near-unity selectivity and high mass activity, ACS Appl. Energy Mater. 5 (2022) 14779–14788, https://doi.org/10.1021/acsaem.2c02143.

[6] J. Wang, Z. Zhu, Y. Lin, Z. Li, W. Tang, J. Wang, J.S. Chen, R. Wu, Nano-engineering in zinc-based catalysts for CO_2 electroreduction: advances and challenges, Carbon Neutralization 3 (2024) 423–440, https://doi.org/10.1002/cnl2.131.

[7] Y.-P. Huang, C.-W. Tung, T.-L. Chen, C.-S. Hsu, M.-Y. Liao, H.-C. Chen, H.M. Chen, *In situ* probing the dynamic reconstruction of copper–zinc electrocatalysts for CO_2 reduction, Nanoscale 14 (2022) 8944–8950, https://doi.org/10.1039/D2NR01478E.

[8] D.L.T. Nguyen, M.S. Jee, D.H. Won, H. Jung, H.-S. Oh, B.K. Min, Y.J. Hwang, Selective CO_2 reduction on zinc electrocatalyst: the effect of zinc oxidation state induced by pretreatment environment, ACS Sustain. Chem. Eng. 5 (2017) 11377–11386, https://doi.org/10.1021/acssuschemeng.7b02460.

[9] M.P.L. Kang, M.J. Kolb, F. Calle-Vallejo, B.S. Yeo, The role of undercoordinated sites on zinc electrodes for CO_2 reduction to CO, Adv. Funct. Mater. 32 (2022) 2111597, https://doi.org/10.1002/adfm.202111597.

[10] M.A.O. Lourenço, J. Zeng, P. Jagdale, M. Castellino, A. Sacco, M.A. Farkhondehfal, C.F. Pirri, Biochar/zinc oxide composites as effective catalysts for electrochemical CO_2 reduction, ACS Sustain. Chem. Eng. 9 (2021) 5445–5453, https://doi.org/10.1021/acssuschemeng.1c00837.

[11] I. Stamatelos, C.-T. Dinh, W. Lehnert, M. Shviro, Zn-based catalysts for selective and stable electrochemical CO_2 reduction at high current densities, ACS Appl. Energy Mater. 5 (2022) 13928–13938, https://doi.org/10.1021/acsaem.2c02557.

[12] R. Wang, Y. Peng, J. Chung, Z. Chen, X. Wang, H. Yin, Y.A. Wu, J. Luo, J. Li, Understanding of C=O bonding activation during CO2 electroreduction: a case study of CO2 reduction to CO on ZnO, Chem. Catal. 3 (2023) 100792, https://doi.org/10.1016/j.checat.2023.100792.

[13] H. Wang, Y. Xiao, Y. Qi, A. Zhang, J. Du, J. Li, T. Guo, Fabrication of ZnO nanosheets self-assembled by nanoparticles for accelerated electrocatalytic reduction of CO2 to CO, Fuel 333 (2023) 126431, https://doi.org/10.1016/j.fuel.2022.126431.

[14] W. Luo, Q. Zhang, J. Zhang, E. Moioli, K. Zhao, A. Züttel, Electrochemical reconstruction of ZnO for selective reduction of CO2 to CO, Appl. Catal. B Environ. 273 (2020) 119060, https://doi.org/10.1016/j.apcatb.2020.119060.

[15] L.R. Manpatilan, S. Bianco, G. Cicero, J. Zeng, E.M. Tresso, Vapor deposition strategies for copper-based electrocatalysts in CO_2 reduction applications, ChemSusChem 2500813 (2025), https://doi.org/10.1002/cssc.202500813.

[16] J.D. Lenef, S.Y. Lee, K.M. Fuelling, K.E. Rivera Cruz, A. Prajapati, D.O. Delgado Cornejo, T.H. Cho, K. Sun, E. Alvarado, T.S. Arthur, C.A. Roberts, C. Hahn, C.C. L. McCrory, N.P. Dasgupta, Atomic layer deposition of Cu electrocatalysts on gas diffusion electrodes for CO $_2$ reduction, Nano Lett. 23 (2023) 10779–10787, https://doi.org/10.1021/acs.nanolett.3c02917.

[17] C. Liu, C. Wang, C. Kei, Y. Hsueh, T. Perng, Atomic layer deposition of platinum nanoparticles on carbon nanotubes for application in proton-exchange membrane fuel cells, Small 5 (2009) 1535–1538, https://doi.org/10.1002/smll.200900278.

[18] S.Y. Lee, J.D. Lenef, D.O. Delgado Cornejo, A.M. Ortiz-Ortiz, T. Ma, T.S. Arthur, C. A. Roberts, N.P. Dasgupta, Tuning the selectivity of bimetallic Cu electrocatalysts for CO_2 reduction using atomic layer deposition, Chem. Commun. 61 (2025) 965–968, https://doi.org/10.1039/D4CC04820B.

[19] B. Bawab, J. Rodriguez-Pereira, J. Michalička, M. Pouzar, L. Hromadko, R. Zazpe, J.M. Macak, Atomic layer deposited Ir nanostructures on titania nanotube layers for efficient alkaline hydrogen evolution reaction, Electrochim. Acta 535 (2025) 146607, https://doi.org/10.1016/j.electacta.2025.146607.

[20] S. Shin, Z. Jin, D.H. Kwon, R. Bose, Y.-S. Min, High turnover frequency of hydrogen evolution reaction on amorphous MoS_2 thin film directly grown by atomic layer deposition, Langmuir 31 (2015) 1196–1202, https://doi.org/10.1021/la504162u.

[21] K.L. Pickrahn, S.W. Park, Y. Gorlin, H. Lee, T.F. Jaramillo, S.F. Bent, Active MnO_x electrocatalysts prepared by atomic layer deposition for oxygen evolution and oxygen reduction reactions, Adv. Energy Mater. 2 (2012) 1269–1277, https://doi.org/10.1002/aenm.201200230.

[22] H. Li, Z. Guo, X. Wang, Atomic-layer-deposited ultrathin Co_9S_8 on carbon nanotubes: an efficient bifunctional electrocatalyst for oxygen evolution/reduction reactions and rechargeable Zn–air batteries, J. Mater. Chem. A 5 (2017) 21353–21361, https://doi.org/10.1039/C7TA06243E.

[23] C.-T. Hsieh, D.-Y. Tzou, M.-T. Jiang, Methanol electro-oxidation on Pt nanocatalysts prepared by atomic layer deposition, J. Electroanal. Chem. 794 (2017) 139–147, https://doi.org/10.1016/j.jelechem.2017.04.020.

[24] J. Yang, A. Bahrami, X. Ding, S. Lehmann, N. Kruse, S. He, B. Wang, M. Hantusch, K. Nielsch, Characteristics of ALD-ZnO thin film transistor using H_2O and H_2O_2 as oxygen sources, Adv. Mater. Inter. 9 (2022) 2101953, https://doi.org/10.1002/admi.202101953.

[25] R. Pietruszka, B.S. Witkowski, E. Zielony, K. Gwozdz, E. Placzek-Popko, M. Godlewski, ZnO/Si heterojunction solar cell fabricated by atomic layer deposition and hydrothermal methods, Sol. Energy 155 (2017) 1282–1288, https://doi.org/10.1016/j.solener.2017.07.071.

[26] S.I. Boyadjiev, V. Georgieva, R. Yordanov, Z. Raicheva, I.M. Szilágyi, Preparation and characterization of ALD deposited ZnO thin films studied for gas sensors, Appl. Surf. Sci. 387 (2016) 1230–1235, https://doi.org/10.1016/j.apsusc.2016.06.007.

[27] M.-J. Chen, J.-R. Yang, M. Shiojiri, ZnO-based ultra-violet light emitting diodes and nanostructures fabricated by atomic layer deposition, Semicond. Sci. Technol. 27 (2012) 074005, https://doi.org/10.1088/0268-1242/27/7/074005.

[28] A. Di Mauro, M. Cantarella, G. Nicotra, V. Privitera, G. Impellizzeri, Low temperature atomic layer deposition of ZnO: applications in photocatalysis, Appl. Catal. B Environ. 196 (2016) 68–76, https://doi.org/10.1016/j.apcatb.2016.05.015.

[29] B. Paul, A. Bahrami, V. Hahn, A. Quade, A. Datye, K. Kosiba, S. Pilz, P. Goldberg, U. D. Schwarz, F. Hempel, J. Hufenbach, K. Nielsch, Atomic layer deposition of ZnO coating on biodegradable Fe-based alloys, Adv. Mater. Inter. 12 (2025) 2400895, https://doi.org/10.1002/admi.202400895.

[30] D. Ren, J. Gao, L. Pan, Z. Wang, J. Luo, S.M. Zakeeruddin, A. Hagfeldt, M. Grätzel, Atomic layer deposition of ZnO on CuO enables selective and efficient electroreduction of carbon dioxide to liquid fuels, Angew. Chem. Int. Ed. 58 (2019) 15036–15040, https://doi.org/10.1002/anie.201909610.

[31] J.W. Elam, S.M. George, Growth of ZnO/Al_2O_3 alloy films using atomic layer deposition techniques, Chem. Mater. 15 (2003) 1020–1028, https://doi.org/10.1021/cm020607+.

[32] A.A. Ahmad, A.M. Alsaad, I.A. Aljarrah, Q.M. Al-Bataineh, A.D. Telfah, Optical, electronic, and structural properties of different nanostructured ZnO morphologies, Eur. Phys. J. 137 (2022) 752, https://doi.org/10.1140/epjp/s13360-022-02967-2.

[33] W.-Z. Fang, Y.-Q. Tang, C. Ban, Q. Kang, R. Qiao, W.-Q. Tao, Atomic layer deposition in porous electrodes: a pore-scale modeling study, Chem. Eng. J. 378 (2019) 122099, https://doi.org/10.1016/j.cej.2019.122099.

[34] W. Szmyt, C. Guerra-Nuñez, L. Huber, C. Dransfeld, I. Utke, Atomic layer deposition on porous substrates: from general formulation to fibrous substrates and scaling laws, Chem. Mater. 34 (2022) 203–216, https://doi.org/10.1021/acs.chemmater.1c03164.

[35] J.D. Henderson, S.D.C. Buchanan, L.H. Grey, M.C. Biesinger, Zinc and cadmium: XPS chemical state determination and auger peak curve-fitting procedures, Appl. Surf. Sci. 730 (2026) 166284, https://doi.org/10.1016/j.apsusc.2026.166284.

[36] G.O. Larrazábal, P. Strøm-Hansen, J.P. Heli, K. Zeiter, K.T. Therkildsen, I. Chorkendorff, B. Seger, Analysis of mass flows and membrane cross-over in CO_2 reduction at high current densities in an MEA-type electrolyzer, ACS Appl. Mater. Interfaces 11 (2019) 41281–41288, https://doi.org/10.1021/acsami.9b13081.

[37] W. Liu, H. Dunne, B. Ballotta, A.A. Massie, M.R. Ghaani, K. McKelvey, S. Dooley, CO_2 loss into solution: an experimental investigation of CO_2 electrolysis with a membrane electrode assembly cell, ACS Appl. Energy Mater. 7 (2024) 7712–7723, https://doi.org/10.1021/acsaem.4c01101.

[38] S. Hao, A. Elgazzar, S.-K. Zhang, T.-U. Wi, F.-Y. Chen, Y. Feng, P. Zhu, H. Wang, Acid-humidified CO_2 gas input for stable electrochemical CO_2 reduction reaction, Science 388 (2025) eadr3834, https://doi.org/10.1126/science.adr3834.

[39] J. Winiarski, W. Tylus, K. Winiarska, I. Szczygieł, B. Szczygieł, XPS and FT-IR Characterization of selected synthetic corrosion products of zinc expected in neutral environment containing chloride ions, J. Spectrosc. 2018 (2018) 1–14, https://doi.org/10.1155/2018/2079278.

Data references

L.R. Manpatilan, A. Bardazzi, P. Glatzel, Operando HERFD-XANES of a ZnO Gas Diffusion Electrode for Electrochemical CO2 reduction (Version 1) [Dataset], Eur. Synchrotron Radiat. Facil. (2026). https://doi.org/10.15151/ESRF-DC-2430456163.